Nanoscale

PAPER

View Article Online
View Journal | View Issue

Cite this: *Nanoscale*, 2020, **12**, 19276

Structural evolution of CrN nanocube electrocatalysts during nitrogen reduction reaction†

Zili Ma, [a,b] Jianhong Chen,[b] Dongbao Luo,[a,c] Thomas Thersleff,[b] Richard Dronskowski [a,c] and Adam Slabon *[b]

Received 2nd July 2020,
Accepted 9th September 2020

DOI: 10.1039/d0nr04981f

rsc.li/nanoscale

Metal nitrides have been suggested as prospective catalysts for the electrochemical nitrogen reduction reaction (NRR) in order to obtain ammonia at room temperature under ambient pressure. Herein, we report that templated chromium nitride porous microspheres built up by nanocubes (NCs) are an efficient noble-metal-free electrocatalyst for NRR. The CrN NCs catalyst exhibits both a high stability and NH_3 yield of 31.11 μg h^{-1} $mg_{cat.}^{-1}$ with a Faradaic efficiency (FE) of 16.6% in 0.1 M HCl electrolyte. Complementary physical characterization techniques demonstrate partial oxidation of the pristine CrN NCs during reaction. Structural characterization by means of scanning transmission electron microscopy (STEM) combining electron energy loss spectrum (EELS) and energy dispersive X-ray spectroscopy (EDX) analysis reveals the NC structure to consist of an O-rich core and N-rich shell after NRR. This gradient distribution of nitrogen within the CrN NCs upon completed NRR is distinct to previously reported metal nitride NRR catalysts, because no significant loss of nitrogen occurs at the catalyst surface.

Introduction

Shortening of energy supplies combined with an increasing environmental pollution have become the major restriction factors in the sustainable development of human society.[1,2] These call for the urgent demand of renewable energy and green synthesis of important chemicals. NH_3 is not only a vital chemical substance to medicine, agriculture, and textiles, but also an attractive carbon-neutral energy carrier with high-energy density.[3,4] Today, NH_3 synthesis is dominated by the industrial Haber–Bosch process, which is usually performed at high temperature and pressure with heavy energy consumption.[5,6] Additionally, the high emission of CO_2 that are inevitable connected with the Haber–Bosch process force the chemical industry to search for carbon-neutral alternatives with respect to legislative regulations on CO_2 emission trading certificates.[7,8]

Reducing N_2 to NH_3 in aqueous systems under ambient conditions and an external voltage, *i.e.* electrocatalytic NRR, has been identified as a potential feasible solution by theoretical studies and previous experimental work.[9,10] During the NRR, NH_3 is produced by activation of atmospheric nitrogen and by using water molecules as the hydrogen source.[11,12] However, its practical application is still hindered by various factors, such as the low NH_3 generation rate and low Faradaic efficiency (FE) values. An efficient catalyst for the NRR is required in order to overcome large overpotential due to the strongly covalent N≡N bonds and poor polarizability of the N_2 molecule.[13] It is therefore crucial to develop an electrocatalyst that combines high FE with sufficient stability. During the last few years, numerous materials have been investigated as potential electrocatalysts for NRR under ambient conditions in aqueous solutions.[14–16] Among the two typical NRR electrocatalysts, *i.e.* homogeneous and heterogeneous entities, the latter is more beneficial with respect to lower cost, higher durability and easier integration with electrode support materials.[17] The most investigated noble-metal catalysts, such as Pt and Rh, are naturally limited due their scarcity, high price and the strong competitive reaction of hydrogen evolution reaction (HER).[18] It has been proven theoretically and experimentally that a relatively strong interaction with N_2 as well as a weak binding to intermediate species, in combination with a relatively low proton adsorption ability to suppress the competing HER, is essential for a NRR electrocatalyst.[19]

[a]*Chair of Solid-State and Quantum Chemistry, Institute of Inorganic Chemistry, RWTH Aachen University, 52056 Aachen, Germany*
[b]*Department of Materials and Environmental Chemistry, Stockholm University, 10691 Stockholm, Sweden. E-mail: adam.slabon@mmk.su.se*
[c]*Hoffmann Institute of Advanced Materials, Shenzhen Polytechnic, 7098 Liuxian Boulevard, Nanshan District, Shenzhen, China*

†Electronic supplementary information (ESI) available. See DOI: 10.1039/d0nr04981f

To date, transition-metal oxides (TMOs) such as WO_3,[20] Ta_2O_5 [21] and CeO_2 [22] containing metal ions with noble-gas electronic shells have been broadly applied as electrocatalysts for NRR under ambient conditions because of their availability.[23] However, the unfavorable adsorption of N_2 due to their electron-rich surface and low FE due to poor conductivity is hindering their application severely.[24] Thus, research has been devoted to other non-oxide transition-metal-based materials to find new candidates for the NRR, such as 2D MXenes,[25] metal carbides,[26] metal complexes in nitrogen-doped carbon,[27] metal sulphides,[28] metal nitrides,[29–32] metal hydrides,[33] metal halogens[34] and perovskite oxynitride-hydrides.[35] Besides that, the metal-free carbon nitride also has been proposed.[36] Among them, recent theoretical calculations[10,37] and experimental results[30,31] have proposed that transition-metal nitrides are promising electrocatalyst candidates for NRR, operating *via* the Mars-van Krevelen (**MvK**) mechanism under ambient conditions. The key feature of Mvk mechanism is the substitution and exchange of atoms from the catalyst's lattice by the adsorbed reactants, forming consequently the product which contains the elements from both the feed reactants and the catalyst. Scheme 1 illustrates one possible pathway of the MvK mechanism for the NRR over transition-metal nitride electrocatalysts.[30,31]

The electrode–electrolyte interface is the key parameter for NH_3 electrosynthesis due to N_2 activation and the competing HER.[38] The majority of non-noble metal catalysts undergo significant chemical changes during NRR, such as partial substitution of the anion (*e.g.* VN to VO_xN_y [30]) or loss of nitrogen (*e.g.* conversion of CrN to Cr_2N [31]). It should be noted that Simonov *et al.* reported that VN is not active for the NRR and that the formed NH_3 is due to loss of surface nitrogen of the catalyst; *i.e.* leaving a stable nitride core and a mixed nitride-oxide shell upon electrochemical operation.[39] ^{15}N isotope experiments have revealed that VN reduces nitrogen *via* the MvK mechanism. Further quantitative $^{14}N/^{15}N$ isotope-exchange experiments determined the density of active surface N atoms on the vanadium nitride electrocatalyst for NRR.[40] Accordingly, metal nitride electrocatalysts should display a stable nitride core and a mixed nitride-oxide shell upon electrochemical operation conditions for NRR. However, the N/O distribution over these metal nitride particles, which is essential for universal metal nitrides, remains still unclear.

Herein, we report on CrN nanocube (**NC**) electrocatalysts and the observation of an unexpected structural feature during NRR. CrN NCs exhibit an core–shell structure with a nitrogen-rich surface and an oxygen-rich core during NRR; as evidenced by Scanning Transmission Electron Microscopy (STEM) including Electron Energy Loss spectroscopy (EELS) and Energy Dispersive X-ray Spectroscopy (EDX).

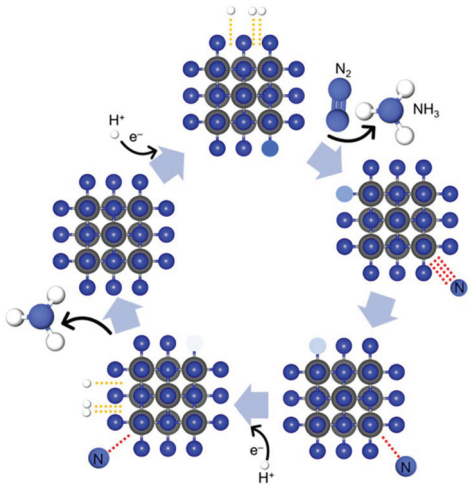

Scheme 1 Schematic illustration of possible pathway of MvK mechanism for NRR reaction over transition-metal nitride electrocatalysts. In the first step, N_2 is being adsorbed on the CrN surface while the NH_3 molecule, which was formed in the previously completed catalytic cycle, desorbs from the catalyst's surface.[30,31]

Experimental section

Preparation of CrN NCs

A glucose-assisted hydrothermal synthesis followed by nitridation was employed to grow CrN NCs (Scheme 2). Briefly, 1 mmol $CrCl_3{\cdot}6H_2O$ (Merck, extra pure) and 25 mmol glucose monohydrate (Grüssing GmbH) were dissolved in 40 ml distilled water by stirring to obtain a clear solution. 10 ml of the solution were added to a 20 mL stainless steel autoclave. The autoclave was sealed and heated at 453 K for 12 h.[41] After the reaction, the autoclave was cooled down to room temperature. The black product was collected and washed with deionized water and ethanol and dried at 333 K for overnight. Then the dried sample was annealed at 773 K for 4 h to obtain Cr_2O_3 microspheres which consist of nanoparticles. Black CrN NCs were obtained by nitridation under flow of NH_3 (15 mL min^{-1}) and H_2 (5 mL min^{-1}) at 1123 K for 8 h.[42] For comparison, pristine CrN was also obtained by nitridation of commercially-available Cr_2O_3 for comparison.

Structural characterization

Powder X-ray diffraction (XRD) patterns were recorded on a STOE STADI-P diffractometer (Cu $K_{\alpha1}$ radiation) equipped with a DECTRIS Mythen 1 K detector in transmission mode. Scanning electron microscopy (SEM) images were acquired

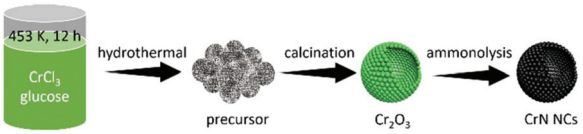

Scheme 2 Schematic illustration of the synthetic procedure for the CrN NCs. Glucose is used as template for preparation of microspheres with an inherent porous structure formed by NCs.

using a Zeiss/LEO 1530. High-resolution transmission electron microscopy (HR-TEM) was conducted on a Themis Z TEM (Thermo Fisher). Electron energy loss spectrum was obtained in scanning transmission electron microscopy (STEM) mode.

Working electrode preparation

Carbon paper (CP) (QuinTech) was washed with deionized water and ethanol for 30 min by sonication. The homogeneous electrocatalyst ink was prepared by dispersing 6 mg CrN NCs in 30 μL of Nafion D-520 dispersion solution (Sigma-Aldrich, 5 wt%) and 970 μL of absolute ethanol by sonicating for 1 h. 20 μL electrocatalyst ink was loaded onto the pre-cleaned carbon paper with area of 1 × 1 cm^2 and dried under ambient condition.

Determination of ammonia

The NH_3 concentrations were determined at 655 nm by means a 20 Genesys spectrophotometer (Spectronic Instruments) using a one-centimeter quartz cuvette and MColortest Ammonium Test kits (Merck, 114750). The standard concentration-absorbance curve was calibrated using the standard NH_4Cl solution with NH_3 concentrations of 0.0, 0.05, 0.10, 0.15, 0.20, 0.25 and 0.30 μg mL^{-1} in 0.1 M HCl. Typically, 4500 μL standard solution was mixed with 450 μL 1 M NaOH (Th. Geyer GmbH) to adjust the pH within the required range 4–13. Then, 0.4 mL reagent NH_4-1 and 1 level microspoon reagent NH_4-2 were added the above solution under vigorously shaking until the reagent dissolved completely. After waiting 5 min, four drops of reagent NH_4-3 were added. The distilled water was used as the blank sample. The absorbance was measured at 655 nm after exactly 7 min. The fitting curve Fig. S1† ($y = 0.4293x + 0.0589$, $R^2 = 0.997$) showed a good linear relation of absorbance value with the NH_3 concentration. 4500 μL electrolyte was removed from the cathodic chamber for NH_3 determination according this procedure. The NH_3 yield rate and Faradaic efficiency (FE) were calculated using the following equation:

$$\mathrm{NH_3\ yield} = \frac{c_{\mathrm{NH_3}} \times V}{t \times m_{\mathrm{cat.}}}$$

$$\mathrm{FE} = \frac{3 \times F \times c_{\mathrm{NH_3}} \times V}{17 \times Q}$$

where c_{NH3} is the measured concentration of NH_3, V is the volume of the cathodic reaction electrolyte, t is the reaction time, $m_{cat.}$ is the mass of catalyst loaded on the working electrode, F is the Faraday constant and Q is the total charge used for the electrodes.

Determination of N_2H_4

The N_2H_4 concentrations were determined at 455 nm by means a 20 Genesys spectrophotometer (Spectronic Instruments) using a one-centimeter quartz cuvette and Hydrazine Test kits (Merck, 109711). The standard concentration-absorbance curve was calibrated using the standard $N_2H_4{\cdot}H_2SO_4$ solution with N_2H_4 concentrations of 0.00, 0.20, 0.40, 0.60, 0.80 and 1.00 μg mL^{-1} in 0.1 M HCl. Typically, 2300 μL standard solution was mixed with 230 μL 1 M NaOH (Th. Geyer GmbH) to adjust the pH within the required range 2–10 according the test kit manual. Then, 1.0 mL reagent Hy-1 was mixed with the above solution. The distilled water was used as the blank sample. The absorbance was measured at 455 nm after exactly 5 min. The fitting curve Fig. S2† ($y = 1.1151x + 0.0104$, $R^2 = 0.999$) showed a good linear relation of absorbance value with the N_2H_4 concentration. 2300 μL electrolyte was removed from the cathodic chamber for N_2H_4 determination according the above procedure.

Electrochemical measurements

The two-compartment cell (Fig. S3†) separated by a Nafion 117 membrane was used for electrochemical NRR experiments. The electrolyte in the anode and cathode chamber were 50 mL 0.1 M HCl for each compartment. Electrochemical measurements were performed under ambient conditions in a three-electrode setup with an Interface 1010T Workstation (Gamry, USA). A graphite rod and a 1 M Ag/AgCl electrode were used as counter and reference electrodes, respectively. The carbon paper with or without sample were used as working electrode. All current values were recorded *versus* 1 M Ag/AgCl and converted to the reversible hydrogen electrode (RHE) according to E_{RHE} (V) = $E_{\mathrm{Ag/AgCl}}$ + (0.059 × pH) + $E^{\theta}_{\mathrm{Ag/AgCl}}$, and the presented current density was normalized to the geometric surface area. Before collecting data, the working electrodes were subject for chronoamperometry (**CA**) at −0.5 V *vs.* RHE for two hours under N_2 bubbling. Polarization curves were obtained using linear sweep voltammetry (**LSV**) with a scan rate of 5 mV s^{-1} in 0.1 M HCl solution, which was purged with N_2 or Ar for 40 min before the measurement. Before all NRR measurements, fresh electrolyte was purged with N_2 for 30 min. CA measurements were carried out in N_2-saturated 0.1 M HCl solution with continuous N_2 bubbling. For comparison, CA measurements in Ar-saturated 0.1 M HCl solution with continuous Ar bubbling were also conducted.

Computational methods

The Vienna *Ab initio* Simulation Package (VASP)[43] based on density-functional theory and the projector augmented wave (PAW)[44,45] method was used to optimize the structures, also including a dispersion correction (DFT-D3).[46] The exchange–correlation functional was described by the generalized-gradient approximation (GGA) as envisioned by Perdew–Burke–Ernzerhof (PBE).[47] A plane-wave basis-set cutoff of 600 eV and the Γ-point were found to converge energies to smaller than 0.01 eV per atom. In detail, a cubic $Cr_{63}N_{62}{}^{3+}$ crystal with a lattice parameter of 4.1668 Å was put into the center of a cubic 26 × 26 × 26 $Å^3$ simulation cell, and the center Cr atom on the [001] plane with fivefold N coordination was approached by an N–N dimer whose outer N atom was allowed to structurally relax.

Results and discussion

The Cr_2O_3 microspheres precursors were prepared by a modified glucose-mediated-hydrothermal-calcination route.[41] The powder XRD patterns of the synthesized microspheres are presented in Fig. S4,† in accordance with the Cr_2O_3 standard pattern (ICSD 75577). The CrN NCs were synthesized by nitridation of the as-prepared Cr_2O_3 microspheres under continuous flow of NH_3 and H_2. As depicted in Fig. 1, all Bragg peaks can be well indexed to characteristic reflection patterns of CrN (ICSD 152809), revealing a cubic rock-salt structure (Fig. 1b). The complementary bulk CrN were also obtained by nitridation of commercial Cr_2O_3 for comparison (XRD patterns shown in Fig. 1a). Glucose has been employed as the common mediator to produce hollow metal oxides microspheres due the decomposition of carbon core during the calcination step. The SEM images (Fig. 1) reveal that the surface of the microspheres is roughened and formed by aggregated nanoparticles of the metal oxides/nitrides, inducing an inherent porosity of the shell.[48] When comparing the SEM micrographs in Fig. 1c d, more cracks can be observed for CrN NCs than for Cr_2O_3 particles; a phenomenon generally known when nitridation at higher temperatures is carried out.

The carbon paper loaded with the prepared CrN NCs served as cathodic working electrode. The electrocatalytic NRR activity of the sample was evaluated in 0.1 M HCl under ambient conditions in a three-electrode system using a two-compartment cell separated by a Nafion 117 membrane. In the cathode chamber, N_2 gas spreads to the electrode surface, providing the possibility to react with protons provided by the electrolyte solution.[49] The LSV technique was first carried out to explore the electrocatalytic NRR properties. As presented in Fig. 2, the curves in N_2- and Ar-saturated electrolyte have the same shape. It can be seen that the current density in N_2-saturated solution

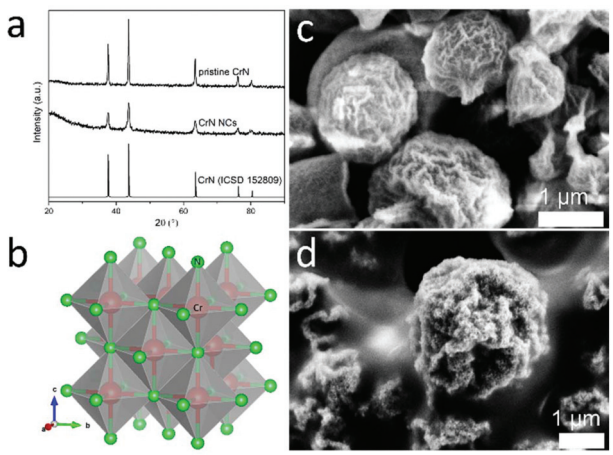

Fig. 1 (a) Experimental and simulated powder XRD patterns of as-prepared CrN (ICSD 152809). Pristine CrN relates to the sample obtained by nitridation of commercial Cr_2O_3 powder. (b) Crystal structure of CrN. (c) SEM micrograph of Cr_2O_3 microspheres precursor. (d) SEM micrograph of final CrN NCs assembled into an electrode.

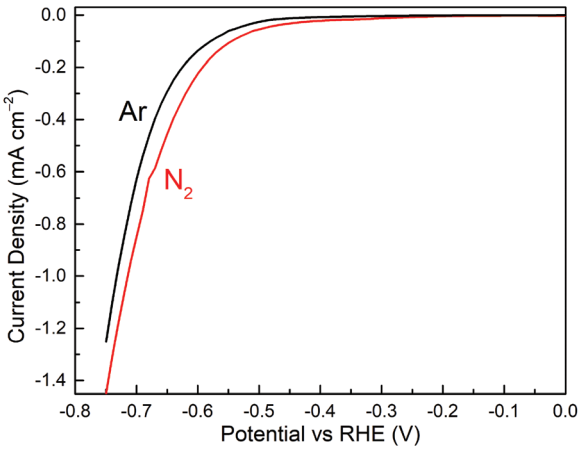

Fig. 2 LSV curves of NCs CrN/CP recorded in N_2-saturated (red line) and Ar-saturated (black line) 0.1 M HCl.

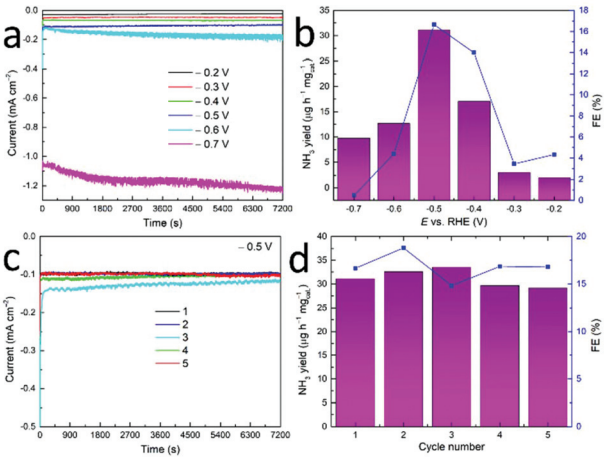

Fig. 3 (a) CA curves of CrN NCs at various potentials for 2 hours in N_2-saturated 0.1 M HCl. (b) NH_3 yields and FE of CrN NCs for the NRR at various potentials. (c) CA curves of CrN NCs for the NRR stability test at a potential of −0.5 V *vs.* RHE for 5 cycles. (d) NH_3 yields and FEs at potential of −0.5 V *vs.* RHE during 5 recycling tests.

is higher than for the Ar-saturated solution at potentials more negative than −0.3 V *vs.* RHE. This indicates that the CrN NCs are active to catalyze the NRR to NH_3.

The electrocatalytic NRR experiments at different potentials were performed for 2 h under a continuous N_2 stream to the cathode chamber. Fig. 3a depicts that the current density remains stable during CA for CrN NCs at various potentials, denoting its stability for the NRR. No N_2H_4 was detected at all applied potentials which hints toward the high selectivity for NH_3 production. Fig. 3b depicts the corresponding NH_3 yields and FEs which were determined *via* the calibration curves. With the potential being more cathodic, both the NH_3 yields and FEs increase and reach the maximum value of 31.11 μg h^{-1} $mg_{cat.}^{-1}$ and FE of 16.64% at −0.5 V *vs.* RHE.

After the applied potential is more cathodic than the volcanic potential, both the NH_3 yields and FEs of electrocatalysts

Table 1 Summary of representative reports on electrocatalytic NRR at ambient conditions

Catalyst	Electrolyte	NH_3 yield	FE(%)	Ref.
CrN NCs	0.1 M HCl	31.11 μg h^{-1} $mg_{cat.}^{-1}$	16.64	This
Mo_2N	0.1 M HCl	78.4 μg h^{-1} $mg_{cat.}^{-1}$	4.5	29
$CrO_{0.66}N_{0.56}$	1 mM H_2SO_4	15.56 μg h^{-1} $mg_{cat.}^{-1}$	6.7	50
AuCo alloy@GO	0.5 M K_2SO_4	36.68 μg h^{-1} $mg_{cat.}^{-1}$	22.08	51
$TiO_2/Ti_3C_2T_x$	0.1 M HCl	32.17 μg h^{-1} $mg_{cat.}^{-1}$	16.07	52
Carbon nitride	0.1 M HCl	8.09 μg h^{-1} $mg_{cat.}^{-1}$	11.59	53
Boron carbide	0.1 M HCl	26.57 μg h^{-1} $mg_{cat.}^{-1}$	15.95	54
Au-Ti_3C_2	0.1 M HCl	30.06 μg h^{-1} $mg_{cat.}^{-1}$	18.34	55
SA-Ag/NC	0.1 M HCl	270.9 μg h^{-1} $mg_{cat.}^{-1}$	21.9	56
Co–N_x–C	0.05 M H_2SO_4	37.6 μg h^{-1} $mg_{cat.}^{-1}$	17.6	57

begin to decrease considerably. These results might attribute to the competitive hydrogen-evolving process and adsorption of N_2 and hydrogen species on the electrode surface.[58] Therefore, the optimum potential of −0.5 V *vs.* RHE was selected for further studies in this system. The NH_3 and FE were compared with other catalysts (see Table 1 and Table S1†), suggesting CrN presented comparable performance to other common catalyst but lower than that of a single atom catalyst. One chromium nitride-based material ($CrO_{0.66}N_{0.56}$) for NRR has been carried out by Shao and co-workers.[39] In their work, the NH_3 yield of 15.56 μg h^{-1} $mg_{cat.}^{-1}$ at a cell voltage of 2.0 V and the highest FE of 6.7% at a cell voltage of 1.8 V has been achieved over an home-made proton exchange membrane electrolyzer, in which chromium oxynitride nanoparticles were used as the electrocatalyst at the cathode side and IrO_2 was used as the electrocatalyst at the anode side.

The stability of the CrN NCs during NRR was estimated by means of consecutive recycling tests. Five cycling tests of 2 hours of long-time CA at −0.5 V *vs.* RHE were carried out in this study. Only a slight decrease in current density was observed after five cycling tests (Fig. 3c). The NH_3 yield rate and corresponding FEs of NCs show small changes and no obvious downward trend after reduplicate tests (Fig. 3d), thus implying good catalytic stability for NRR in accordance with previous (oxy)nitrides studies.[50,59]

We also compared the NRR performance of the CrN NCs particles with microcrystalline CrN. Fig. 4a evidences that the NH_3 yield and FE of CrN NCs at −0.5 V *vs.* RHE is higher than that of bulk CrN, *i.e.* approximately 2.9 times larger under the same CA conditions. Possible reasons are the higher concentration of active sites and the diffusion of both reactants and products in the porous structure.[41] To further demonstrate the electrocatalytic activity of CrN NCs for NRR, certain control experiments were also carried out: (i) CrN NCs/CP in N_2-saturated solution at open circuit potential, (ii) CrN NCs/CP in Ar-saturated solution at −0.5 V *vs.* RHE, (iii) CrN NCs/CP in air at −0.5 V *vs.* RHE, (iv) bare CP in N_2-saturated solution at −0.5 V *vs.* RHE and (v) pristine CrN/CP in N_2-saturated solution at −0.5 V *vs.* RHE (see Fig. 4a). During the first four control experiments only negligible NH_3 formation was detected. This confirms that the measured amount of NH_3 in this work was produced mainly from the

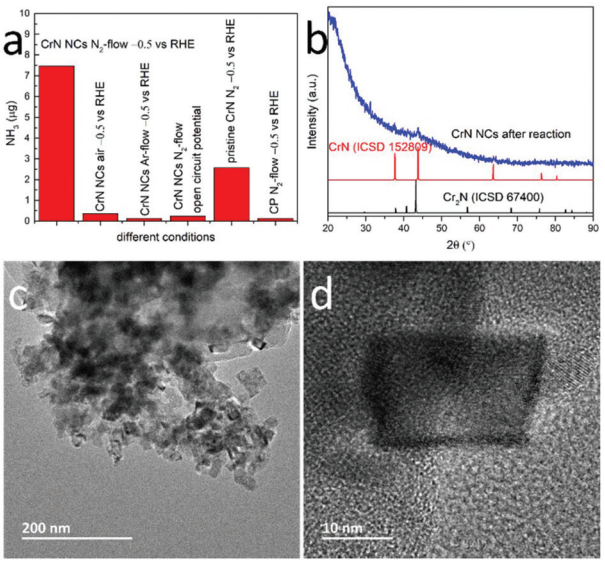

Fig. 4 (a) Comparing NH_3 yields and FE with control experiments. (b) XRD patterns of CrN NCs after NRR and simulated CrN and Cr_2N patterns for comparison. TEM (c) and HR-TEM (d) image of CrN NCs after NRR.

NRR process using N_2 as the nitrogen source and CrN NCs as the electrocatalyst, because the detected catalytically-produced NH_3 amount is significantly higher than the sum from the control experiments.

To understand the reaction process, the CrN NCs were further characterized after a stability test. The recorded powder XRD patterns of the CrN NCs displayed the characteristic reflections for CrN, but with a higher background due to potential amorphization. New Bragg peaks hint toward the formation of a new phase during NRR (Fig. 4b), which is consistent with previous reports on metal nitride NRR electrocatalysts (VN[30] and Cr_2N[31]). Particularly, the metal nitrides NRR electrocatalysts have been reported to partially convert to the oxidic or oxynitridic form, providing evidence for the MvK mechanism in NRR reaction. Partially substituting the nitride anion with an oxide anion has been suggested to improve the electronic properties in order to improve the NRR performance. These results have been proven by means of complementary

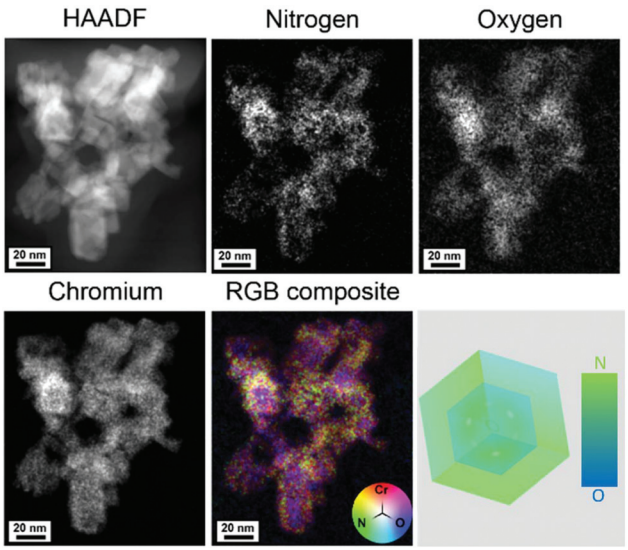

Fig. 5 STEM EDX mapping for CrN NCs after stability test for NRR. The panel at the bottom right depicts the illustration of N and O distributions in a NC. Note the formation of a nitrogen-rich surface layer of the agglomerated NCs.

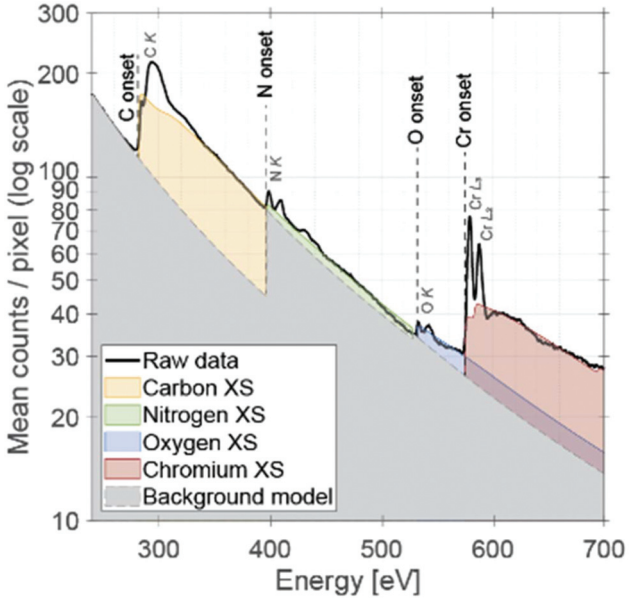

Fig. 6 STEM EEL spectrum of CrN NCs after stability test for NRR. XS stands for cross-section.

physical characterization techniques and density functional theory (DFT) calculations previously.[30]

The morphology of the CrN NCs after NRR is shown in the TEM images in Fig. 4c and d. The NCs display particle sizes of approximately 20 nm, and clear lattice fringes can be observed from the HRTEM images. The chemical composition of the CrN NCs after NRR has been analyzed by STEM spectroscopy combining EDX and EELS. Fig. 5 shows the high-angle annular dark field (HAADF) STEM micrograph of the CrN catalyst after NRR and the corresponding elemental abundance maps obtained from EDX spectroscopy. Chromium is distributed homogenously throughout the particles. The elemental correlation map in Fig. 5 shows a striking feature of the NCs after NRR. Instead of forming a nitrogen-rich core as would be initially expected due to the MvK reaction mechanisms, the CrN NCs evidence the opposite structural feature in the form of a nitrogen-rich surface. Although metal nitrides with a higher nitrogen concentration at the surface have been reported previously,[60] it should be noted that the CrN have been subject to NRR. Since the latter occurs at metal nitrides *via* the MvK mechanism, their surface composition contains oxide anions that substitute nitride anions due to nitrogen leaching.[30,31,40,61]

For the CrN NCs, a possible explanation would be the leaching of the nitrogen atoms upon application of a cathodic current under NRR conditions and a rapid re-nitridation cycle which only occurs at the surface[40] and does not proceed to the core of the NCs. The result is a gradient distribution of nitrogen atoms along the whole diameter of the CrN NC. Chang *et al.* have proposed that a metal oxynitride shell could increase the NRR performance by π backdonation from a delocalized electron environment for nitrogen absorption and activation.[24] For the CrN NCs, an average ratio of Cr : N : O was determined to be 2 : 1 : 1; although this relation does not distinguish between the bulk and surface concentration. Another possible reason for the oxygen-rich core could be the residual oxygen atoms upon conversion of Cr_2O_3 to CrN (see Fig. S5†). However, we believe that this does not explain the nitrogen-rich shell after NRR, because one would expect a loss of nitrogen due to the MvK mechanism. Clearly, this is not the case for the CrN NC catalyst.

Complementary spectroscopic analysis by means of STEM EELS was further performed to confirm the elemental ratio and the oxidation state of Cr (see Fig. 6). Similar elemental ratio was observed as EDX mapping analysis. Based on the qualitative comparison to the literature,[62] it is suggested that Cr has an oxidation state of +3. Recently, Jaramillo and coworkers have shown using the example of MoN that the controlled oxygen incorporation into the surface and bulk is a critical parameter to tailor the catalytic performance for the oxygen reduction reaction.[63] Our results indicate that a similar case is present for the CrN NCs when being used catalysts for the NRR.

For the elucidation of the interaction between the CrN catalyst and N_2 molecule, complementary theoretical analysis at the DFT level has been carried out (Fig. 7). Briefly, a cubic CrN crystal with 125 atoms (*vide supra*) was applied as model system to investigate the interaction with an approaching N_2 molecule. The total-energy minimum results for a N_2–Cr distance of about 2.067 Å and indicates that adsorption of N_2 on CrN is indeed energetically favored. Still, more sophisticated theoretical investigations are required to address the adsorption mechanism of N_2 on the CrN catalyst with respect to different facets in order to model the complete MvK mechanism.

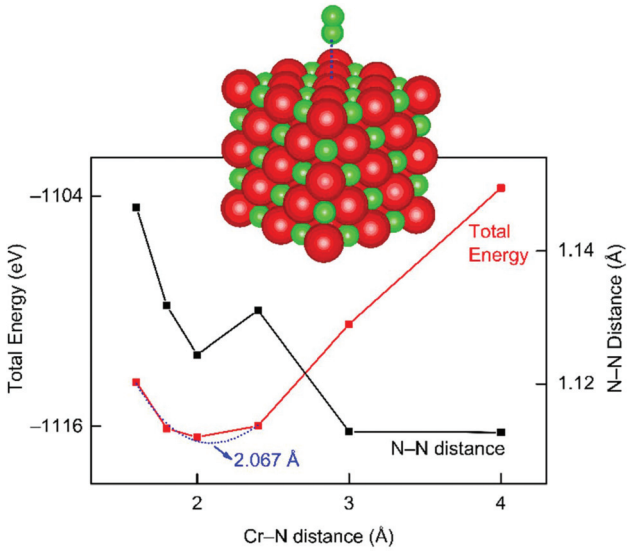

Fig. 7 DFT simulation of molecular N_2 approaching a cubic chromium nitride crystal, with the total energy given in red and the N–N distance in black.

Conclusions

In summary, we have synthesized CrN microspheres assembled from NCs with inherent porosity and investigated the structure at the nanoscale during NRR. As regards their performance, the catalyst has been tested in 0.1 M HCl electrolyte under ambient conditions, achieving an excellent selectivity and a high NH_3 yield of 31.11 μg h^{-1} $mg_{cat.}^{-1}$ with a Faradaic efficiency of 16.6% at −0.5 V *vs.* RHE. Complementary physical characterization techniques demonstrate partial oxidation of the pristine CrN NCs during reaction. Structural characterization by means of EELS and EDX analysis reveals that O-rich core and N-rich shell structure is formed after NRR. This gradient distribution of nitrogen within the CrN catalyst structure upon completed NRR is distinct to previously reported metal nitride NRR catalysts; the latter showing significant loss of nitrogen at the surface. The study not only provides an efficient earth-abundant catalyst for NRR, but also demonstrates the necessity of STEM spectroscopy to understand the critical changes in the chemical nature for metal nitride catalysts at the nanoparticle level. The higher distribution of nitrogen atoms at the surface of the CrN nanocubes, in comparison to its core, indicates that the NRR occurring *via* the MvK mechanism does not necessarily result in significant substitution of nitrogen atoms with oxygen atoms at the surface during reaction.

Conflicts of interest

There are no conflicts to declare.

Acknowledgements

Z. M. thanks the China Scholarship Council for a PhD scholarship. T. T. acknowledges support from the Swedish Research Council (project no. 2016-05113). A. S. would like to thank Vinnova, the Swedish innovation agency, for financial support (project: C1Bio 2019-03174). We thank Birgit Hahn for acquiring the SEM images and Dr Istvan Zoltan-Jenei for fruitful discussions.

Notes and references

1 S. Chu and A. Majumdar, *Nature*, 2012, **488**, 294–303.
2 J. G. Chen, R. M. Crooks, L. C. Seefeldt, K. L. Bren, R. M. Bullock, M. Y. Darensbourg, P. L. Holland, B. Hoffman, M. J. Janik, A. K. Jones, M. G. Kanatzidis, P. King, K. M. Lancaster, S. V. Lymar, P. Pfromm, W. F. Schneider and R. R. Schrock, *Science*, 2018, **360**, eaar6611.
3 V. Rosca, M. Duca, M. T. de Groot and M. T. M. Koper, *Chem. Rev.*, 2009, **109**, 2209–2244.
4 C. Liu, K. K. Sakimoto, B. C. Colón, P. A. Silver and D. G. Nocera, *Proc. Natl. Acad. Sci. U. S. A.*, 2017, **114**, 6450–6455.
5 P. J. Chirik, *Nat. Chem.*, 2009, **1**, 520–522.
6 K. Honkala, *Science*, 2005, **307**, 555–558.
7 N. Lazouski, M. Chung, K. Williams, M. L. Gala and K. Manthiram, *Nat. Catal.*, 2020, **3**, 463–469.
8 C. Ampelli, *Nat. Catal.*, 2020, **3**, 420–421.
9 Y.-C. Hao, Y. Guo, L.-W. Chen, M. Shu, X.-Y. Wang, T.-A. Bu, W.-Y. Gao, N. Zhang, X. Su, X. Feng, J.-W. Zhou, B. Wang, C.-W. Hu, A.-X. Yin, R. Si, Y.-W. Zhang and C.-H. Yan, *Nat. Catal.*, 2019, **2**, 448–456.
10 Y. Abghoui, A. L. Garden, V. F. Hlynsson, S. Björgvinsdóttir, H. Ólafsdóttir and E. Skúlason, *Phys. Chem. Chem. Phys.*, 2015, **17**, 4909–4918.
11 J. Hou, M. Yang and J. Zhang, *Nanoscale*, 2020, **12**, 6900–6920.
12 G. Qing, R. Ghazfar, S. T. Jackowski, F. Habibzadeh, M. M. Ashtiani, C.-P. Chen, M. R. Smith and T. W. Hamann, *Chem. Rev.*, 2020, **120**, 5437–5516.
13 S. Gao, Y. Zhu, Y. Chen, M. Tian, Y. Yang, T. Jiang and Z. L. Wang, *Mater. Today*, 2019, **28**, 17–24.
14 S. Z. Andersen, V. Čolić, S. Yang, J. A. Schwalbe, A. C. Nielander, J. M. McEnaney, K. Enemark-Rasmussen, J. G. Baker, A. R. Singh, B. A. Rohr, M. J. Statt, S. J. Blair, S. Mezzavilla, J. Kibsgaard, P. C. K. Vesborg, M. Cargnello, S. F. Bent, T. F. Jaramillo, I. E. L. Stephens, J. K. Nørskov and I. Chorkendorff, *Nature*, 2019, **570**, 504–508.
15 Y. Song, D. Johnson, R. Peng, D. K. Hensley, P. V. Bonnesen, L. Liang, J. Huang, F. Yang, F. Zhang, R. Qiao, A. P. Baddorf, T. J. Tschaplinski, N. L. Engle, M. C. Hatzell, Z. Wu, D. A. Cullen, H. M. Meyer, B. G. Sumpter and A. J. Rondinone, *Sci. Adv.*, 2018, **4**, e1700336.

16 A. J. Martín, T. Shinagawa and J. Pérez-Ramírez, *Chem*, 2019, **5**, 263–283.
17 J. Zhao and Z. Chen, *J. Am. Chem. Soc.*, 2017, **139**, 12480–12487.
18 C. Li, Y. Fu, Z. Wu, J. Xia and X. Wang, *Nanoscale*, 2019, **11**, 12997–13006.
19 M. Li, H. Huang, J. Low, C. Gao, R. Long and Y. Xiong, *Small Methods*, 2019, **3**, 1800388.
20 W. Kong, R. Zhang, X. Zhang, L. Ji, G. Yu, T. Wang, Y. Luo, X. Shi, Y. Xu and X. Sun, *Nanoscale*, 2019, **11**, 19274–19277.
21 W. Fu, P. Zhuang, M. O. Chee, P. Dong, M. Ye and J. Shen, *ACS Sustainable Chem. Eng.*, 2019, **7**, 9622–9628.
22 H. Xie, H. Wang, Q. Geng, Z. Xing, W. Wang, J. Chen, L. Ji, L. Chang, Z. Wang and J. Mao, *Inorg. Chem.*, 2019, **58**, 5423–5427.
23 X. Cui, C. Tang, X. Liu, C. Wang, W. Ma and Q. Zhang, *Chem. – Eur. J.*, 2018, **24**, 18494–18501.
24 B. Chang, L. Deng, S. Wang, D. Shi, Z. Ai, H. Jiang, Y. Shao, L. Zhang, J. Shen, Y. Wu and X. Hao, *J. Mater. Chem. A*, 2020, **8**, 91–96.
25 W. Peng, M. Luo, X. Xu, K. Jiang, M. Peng, D. Chen, T. Chan and Y. Tan, *Adv. Energy Mater.*, 2020, 2001364.
26 H. Cheng, L.-X. Ding, G.-F. Chen, L. Zhang, J. Xue and H. Wang, *Adv. Mater.*, 2018, **30**, 1803694.
27 C. He, Z.-Y. Wu, L. Zhao, M. Ming, Y. Zhang, Y. Yi and J.-S. Hu, *ACS Catal.*, 2019, **9**, 7311–7317.
28 X. Li, T. Li, Y. Ma, Q. Wei, W. Qiu, H. Guo, X. Shi, P. Zhang, A. M. Asiri, L. Chen, B. Tang and X. Sun, *Adv. Energy Mater.*, 2018, **8**, 1801357.
29 X. Ren, G. Cui, L. Chen, F. Xie, Q. Wei, Z. Tian and X. Sun, *Chem. Commun.*, 2018, **54**, 8474–8477.
30 X. Yang, J. Nash, J. Anibal, M. Dunwell, S. Kattel, E. Stavitski, K. Attenkofer, J. G. Chen, Y. Yan and B. Xu, *J. Am. Chem. Soc.*, 2018, **140**, 13387–13391.
31 J. Nash, X. Yang, J. Anibal, M. Dunwell, S. Yao, K. Attenkofer, J. G. Chen, Y. Yan and B. Xu, *J. Phys. Chem. C*, 2019, **123**, 23967–23975.
32 J. Zhao, C. Cui, H. Wang, J. Han, X. Zhu and Q. Ge, *J. Phys. Chem. C*, 2020, **124**, 616–624.
33 W. Xu, G. Fan, J. Chen, J. Li, L. Zhang, S. Zhu, X. Su, F. Cheng and J. Chen, *Angew. Chem., Int. Ed.*, 2020, **59**, 3511–3516.
34 Y. Li, T. Li, X. Zhu, A. A. Alshehri, K. A. Alzahrani, S. Lu and X. Sun, *Chem. – Asian J.*, 2020, **15**, 487–489.
35 M. Kitano, J. Kujirai, K. Ogasawara, S. Matsuishi, T. Tada, H. Abe, Y. Niwa and H. Hosono, *J. Am. Chem. Soc.*, 2019, **141**, 20344–20353.
36 G. Peng, J. Wu, M. Wang, J. Niklas, H. Zhou and C. Liu, *Nano Lett.*, 2020, **20**, 2879–2885.
37 Y. Abghoui, A. L. Garden, J. G. Howalt, T. Vegge and E. Skúlason, *ACS Catal.*, 2016, **6**, 635–646.
38 L. Hu, Z. Xing and X. Feng, *ACS Energy Lett.*, 2020, **5**, 430–436.
39 H.-L. Du, T. R. Gengenbach, R. Hodgetts, D. R. MacFarlane and A. N. Simonov, *ACS Sustainable Chem. Eng.*, 2019, **7**, 6839–6850.
40 X. Yang, S. Kattel, J. Nash, X. Chang, J. H. Lee, Y. Yan, J. G. Chen and B. Xu, *Angew. Chem., Int. Ed.*, 2019, **131**, 13906–13910.
41 Y. Zhang, W. Qiu, Y. Ma, Y. Luo, Z. Tian, G. Cui, F. Xie, L. Chen, T. Li and X. Sun, *ACS Catal.*, 2018, **8**, 8540–8544.
42 Y. Li, L. Gao, J. Li and D. Yan, *J. Am. Ceram. Soc.*, 2004, **85**, 1294–1296.
43 G. Kresse and J. Furthmüller, *Phys. Rev. B: Condens. Matter Mater. Phys.*, 1996, **54**, 11169–11186.
44 P. E. Blöchl, *Phys. Rev. B: Condens. Matter Mater. Phys.*, 1994, **50**, 17953–17979.
45 G. Kresse and D. Joubert, *Phys. Rev. B: Condens. Matter Mater. Phys.*, 1999, **59**, 1758–1775.
46 S. Grimme, J. Antony, S. Ehrlich and H. Krieg, *J. Chem. Phys.*, 2010, **132**, 154104.
47 J. P. Perdew, K. Burke and M. Ernzerhof, *Phys. Rev. Lett.*, 1996, **77**, 3865–3868.
48 M.-M. Titirici, M. Antonietti and A. Thomas, *Chem. Mater.*, 2006, **18**, 3808–3812.
49 L. Zhang, X. Ji, X. Ren, Y. Luo, X. Shi, A. M. Asiri, B. Zheng and X. Sun, *ACS Sustainable Chem. Eng.*, 2018, **6**, 9550–9554.
50 Y. Yao, Q. Feng, S. Zhu, J. Li, Y. Yao, Y. Wang, Q. Wang, M. Gu, H. Wang, H. Li, X. Yuan and M. Shao, *Small Methods*, 2019, **3**, 1800324.
51 Q. Wang, G. Zheng, S. Hao, X. Liu, J. Zheng, Y. Wang, Z. Su, N. Xu, Y. He, L. Lei and X. Zhang, *ACS Sustainable Chem. Eng.*, 2020, **8**, 44–49.
52 Y. Fang, Z. Liu, J. Han, Z. Jin, Y. Han, F. Wang, Y. Niu, Y. Wu and Y. Xu, *Adv. Energy Mater.*, 2019, **9**, 1803406.
53 C. Lv, Y. Qian, C. Yan, Y. Ding, Y. Liu, G. Chen and G. Yu, *Angew. Chem., Int. Ed.*, 2018, **57**, 10246–10250.
54 W. Qiu, X.-Y. Xie, J. Qiu, W.-H. Fang, R. Liang, X. Ren, X. Ji, G. Cui, A. M. Asiri, G. Cui, B. Tang and X. Sun, *Nat. Commun.*, 2018, **9**, 3485.
55 D. Liu, G. Zhang, Q. Ji, Y. Zhang and J. Li, *ACS Appl. Mater. Interfaces*, 2019, **11**, 25758–25765.
56 Y. Chen, R. Guo, X. Peng, X. Wang, X. Liu, J. Ren, J. He, L. Zhuo, J. Sun, Y. Liu, Y. Wu and J. Luo, *ACS Nano*, 2020, **14**, 6938–6946.
57 M. Qin, X. Li, G. Gan, L. Wang, S. Fan, Z. Yin and G. Chen, *ACS Sustainable Chem. Eng.*, 2020, **8**, 13430–13439.
58 T. Oshikiri, K. Ueno and H. Misawa, *Angew. Chem., Int. Ed.*, 2016, **55**, 3942–3946.
59 S. Kang, J. Wang, S. Zhang, C. Zhao, G. Wang, W. Cai and H. Zhang, *Electrochem. Commun.*, 2019, **100**, 90–95.
60 W. Lengauer, *Surf. Interface Anal.*, 1990, **15**, 377–382.
61 R. Manjunatha, A. Karajić, H. Teller, K. Nicoara and A. Schechter, *ChemCatChem*, 2020, **12**, 438–443.
62 T. L. Daulton and B. J. Little, *Ultramicroscopy*, 2006, **106**, 561–573.
63 M. E. Kreider, M. B. Stevens, Y. Liu, A. M. Patel, M. J. Statt, B. M. Gibbons, A. Gallo, M. Ben-Naim, A. Mehta, R. C. Davis, A. V. Ievlev, J. K. Nørskov, R. Sinclair, L. A. King and T. F. Jaramillo, *Chem. Mater.*, 2020, **32**, 2946–2960.